Materials Advances

ROYAL SOCIETY OF CHEMISTRY

PAPER

View Article Online
View Journal | View Issue

Cite this: *Mater. Adv.*, 2022, 3, 8449

g-C_3N_4/dendritic fibrous nanosilica doped with potassium for photocatalytic CO_2 reduction†

Sushma A. Rawool,[a] Yusuf Kar[b] and Vivek Polshettiwar *[a]

Received 5th July 2022,
Accepted 16th September 2022

DOI: 10.1039/d2ma00809b

rsc.li/materials-advances

Photocatalytic CO_2 conversion is a promising process for the reduction of CO_2 into useful chemicals and fuels using solar energy. In this work, we have synthesized potassium-doped g-C_3N_4 coated over dendritic fibrous nanosilica (K-CN/DFNS) and studied the photocatalytic CO_2 conversion under visible light illumination. K-CN/DFNS was synthesized by heating KOH-treated melamine in a vacuum-sealed quartz tube by varying the amounts of potassium salt. The scanning electron microscopy images confirmed the coating of potassium-doped g-C_3N_4 over DFNS, while the absorption spectra show extended absorption in the visible region and redshift in the bandgap as compared to the undoped CN/DFNS. XPS analysis further confirms the interaction of potassium ions with g-C_3N_4. During the photocatalytic CO_2 conversion, the selectivity towards the formation of hydrogen (from water splitting) was the highest for the g-C_3N_4 and CN/DFNS catalysts, whereas no hydrogen generation was observed using the potassium-doped catalysts. The highest methane yield observed was 1.7 μmol g^{-1} for g-C_3N_4 in 4 h using K-CN/DFNS-2 (with 6 wt% of potassium ions). The high activity and improved selectivity of K-CN/DFNS were due to the extended absorption in the visible region, better separation of charge carriers, shifting of the conduction band and valence band positions towards positive potentials, and moderate adsorption of CO_2 molecules on its surface.

Introduction

The generation of greenhouse gases is a major concern in order to protect the climate from global warming. Fossil fuels produce a large amount of CO_2 during their burning and an increase in CO_2 level of up to 590 ppm can result in a rise in the global temperature by 1.9 °C.[1] Thus, different methodologies have been developed to tackle the issue of excessive anthropogenic CO_2 in the environment.[2–4] One of the best methods is photocatalytic CO_2 conversion using solar energy, where a photocatalyst harvests solar energy to convert CO_2 into valuable fuels like methane, methanol, formic acid *etc.*, using water as a proton source.[3,4] Different metal oxides, sulfides, nitrides, and oxynitrides have been studied as photocatalysts.[3–6] Among them, metal-free organic polymeric graphitic carbon nitride (g-C_3N_4) has attracted tremendous attention because of its low bandgap of 2.7 eV, its inexpensive, environmentally friendly, and chemically inert nature and also the fact that the reduction potential of CO_2 conversion falls within its bandgap.[7,8] It can be synthesized using nitrogen-rich molecules like urea, melamine, cyanamide, dicyandiamide *etc.*[7–11]

Scheme S1 (ESI†) shows the presence of a different type of nitrogen in g-C_3N_4, which helps in CO_2 adsorption and activation because of the lone pair of electrons present on it. The pyridinic nitrogen group shows Lewis basicity because of the presence of a lone pair of electrons and thus helps in the adsorption and activation of CO_2 molecules.[11] This nitrogen has a higher negative charge as it can retain the lone pair of electrons in a planar structure and thus can bind CO_2 more effectively than other types of nitrogen present in g-C_3N_4. Quaternary graphitic nitrogen shows Lewis acidity as the electrons from its π* antibonding orbital are less accessible for CO_2 binding. Also, the other types of nitrogen species formed during incomplete polymerization, such as terminal -NH_2, -NH groups and N-oxides, exhibit some basicity and thus, g-C_3N_4 is suitable for adsorption and activation of CO_2 molecules.[11] In spite of having these advantages, the photocatalytic activity of g-C_3N_4 is low because of limited light absorption until 450 nm in the visible region of the solar spectrum, high charge recombination rate, and low surface area.[8]

For efficient g-C_3N_4 photocatalyst design, adsorption of CO_2, visible light absorption, and charge carrier separation and transfer to carry out redox reactions are the key factors that need to be considered. Different strategies such as doping of cations or anions, composite formation with different semiconductors, tuning of the morphology, and loading of metal

[a] *Department of Chemical Sciences, Tata Institute of Fundamental Research (TIFR), Mumbai, India*
[b] *Shell Technology Center, Bangalore, India. E-mail: vivekpol@tifr.res.in; Tel: (+91) 8452886556*

† Electronic supplementary information (ESI) available. See DOI: https://doi.org/10.1039/d2ma00809b

nanoparticles have been adopted to modify the structural, electronic and optical properties of g-C_3N_4.[8] Among these, the doping of cations into the g-C_3N_4 matrix offers several advantages, such as tuning the bandgap by creating impurity states and the generation of active sites for trapping of photoexcited electrons and holes.[12] Potassium-doped g-C_3N_4 has been studied for photocatalytic hydrogen generation and dye degradation.[13–17] To the best of our knowledge, CO_2 conversion was barely reported using potassium-doped g-C_3N_4.[18,19] Doping of potassium ions into the matrix of g-C_3N_4 was found to be beneficial in extending absorption in the visible region and efficient separation of charge carriers.[13–17] It was also anticipated that the presence of an alkali metal ion like potassium would help in improving the CO_2 adsorption capacity of g-C_3N_4.[18,19] Sun *et al.*[19] introduced an amino group and intercalated the potassium ion in g-C_3N_4 by post-treatment of g-C_3N_4 and KOH. They reported that the generation of the excess amino group improves CO_2 adsorption and activation and the presence of intercalated potassium ions enhanced the separation and transfer of charge carriers. The methane and CO generation was found to be 5.6 and 5.4 times higher than that of g-C_3N_4, respectively. Recently, Wang *et al.* reported CO generation at the rate of 8 μmol g^{-1} h^{-1} over (2.08 at%) potassium-doped g-C_3N_4.[18] Previously, we reported hydrogen generation using g-C_3N_4 decorated over dendritic fibrous nanosilica (DFNS) and it was found to be seven times higher as compared to that of the pristine g-C_3N_4.[20] The improvement in activity was attributed to the visible light enhancement, efficient separation of charge carriers and high surface area.

In continuation of our work on DFNS-based catalytic systems,[20–24] in this work, we doped potassium ions within the framework of g-C_3N_4 coated over DFNS to further improve the photocatalytic CO_2 conversion. Melamine treated with KOH was used as a precursor for the synthesis of potassium-doped g-C_3N_4. This is the first time that we have reported the synthesis of potassium-doped g-C_3N_4 coated over DFNS using a vacuum-sealed quartz tube. The amount of potassium ions was varied and the modifications in the optical, electronic and structural properties of g-C_3N_4 were assessed by different characterization techniques. The catalysts were investigated for photocatalytic CO_2 conversion under visible light illumination. The changes in the structure of g-C_3N_4 brought by doping with potassium ion and the role of DFNS as the support were investigated and the impact of structural changes was correlated with the photocatalytic property of the sample. Preferential evolution of methane over hydrogen generation was observed using potassium-doped samples.

Experimental

Synthesis

Potassium hydroxide-treated melamine (K-melamine) was synthesized by dispersing potassium hydroxide (KOH) and melamine in distilled water. The solution was stirred for 2 h. The solvent was evaporated to dryness at 80 °C in an oven. The amount of KOH varied from 3.2, 25.5 and 45.5 wt% of melamine. K-melamine (250 mg) and DFNS (500 mg) were mixed well by grinding for 1 h. During grinding, ethanol was added after every 20 min to ensure homogeneous mixing. After grinding, the mixture was kept in an oven at 80 °C for 12 h. The dried sample (86 mg) was transferred to a quartz tube and the tube was evacuated at 0.3–0.6 mbar overnight and then sealed under vacuum. The sealed tube was then heated in two steps, first at 400 °C for 2 h and then at 550 °C for 2 h at a heating rate of 10 °C min^{-1}. After cooling down to room temperature, the tube was broken to obtain a powder catalyst. The detailed synthesis procedure is given in Fig. S1 (ESI†). The sample was washed with water four times to remove the impurities. The samples were referred to as K-CN/DFNS-1, K-CN/DFNS-2 and K-CN/DFNS-3 for 3.2, 25.5 and 45.5 wt% of KOH used during synthesis. Pristine g-C_3N_4 without DFNS and CN/DFNS without K doping were also synthesized as controls using the same protocol.

Characterization

Scanning electron microscopy (SEM) was performed on a Zeiss ULTRA instrument. For sample preparation, powders were dispersed in ethanol with the assistance of sonication and a drop of solution was placed on an aluminum SEM grid. The X-ray diffraction (XRD) patterns were recorded using a Panalytical X'Pert Pro powder X-ray diffractometer using Cu Kα radiation. A fixed amount of sample and KBr were mixed to record the FTIR spectra of the samples using a JASCO FT/IR-4700 instrument. The thermal stability of the samples was evaluated by using thermogravimetric analysis (TGA, Mettler Toledo). TGA was carried out by heating the samples in an alumina pan at a heating rate of 10 °C min^{-1} from 30 °C to 800 °C under an air atmosphere. UV-visible DRS spectra were recorded using a Jasco spectrophotometer (Jasco V-770). Lifetime measurements were carried out by using a femto/picosecond laser as the excitation source and employing the time-correlated single photon counting (TCSPC) technique. For fluorescence lifetime measurements, 1 ps pulses of 732 nm radiation from a Ti-sapphire femto/picosecond laser (Spectra-Physics, Mountain View, CA), pumped by a Nd:YLF laser (Millenia X, Spectra-Physics), were frequency-doubled to 396 nm by using a frequency doubler/triplet (GWU, Spectra-Physics). The fluorescence decay curves were obtained at a laser repetition rate of 4 MHz using a microchannel plate photomultiplier (model R2809u, Hamamatsu Corp.) coupled to a TCSPC setup. The instrument response function (IRF) at 396 nm was obtained using a dilute colloidal suspension of a dried non-dairy creamer. The full width at half-maximum (FWHM) of the IRF was 90 ps and the number of channels used was 1024. All the data were fitted with triexponential fitting. It gives three-lifetime values of τ_1, τ_2 and τ_3 corresponding to amplitudes, *A*1, *A*2 and *A*3, respectively. Average lifetime (τ_{avg}) was determined by using the following equation:[26]

$$\tau_{avg} = \frac{A_1 \times \tau_1^2 + A_2 \times \tau_2^2 + A_3 \times \tau_3^2}{A_1 \times \tau_1 + A_2 \times \tau_2 + A_3 \times \tau_3} \quad (1)$$

The surface area was calculated by applying Brunauer–Emmett–Teller (BET) theory to N_2 physisorption data, which was recorded using a Micromeritics Flex3 analyzer. Approximately 100 mg

of each sample was degassed at 120 °C for 12 h prior to N_2 sorption analysis. CO_2 adsorption of the catalyst was studied using a Micromeritics Flex3 analyzer at 25 °C.

The XPS analysis of the sample was done using monochromated Al-Kα radiation (1486.6 eV) as an X-ray source. The carbon signal at 284.6 eV was used as an internal reference. Peak fitting of the spectra was performed using XPSPEAK 4.1 software. The relative positions of the valence band (E_{VB}) and conduction band (E_{CB}) against NHE were calculated from the XPS valence band spectra:[27]

E_{VB} against NHE is estimated using the following equation:

$$E_{VB} = \Delta E - E_{Vac} + W_s \quad (2)$$

where ΔE, E_{VAC} and W_S are the difference between the Fermi level and the valence band maximum, the vacuum level (4.5 eV), and the work function of g-C_3N_4 (4.0 eV), respectively.

E_{CB} is estimated using the following equation:

$$E_{CB} = E_{VB} - E_G \quad (3)$$

where E_G is the bandgap value derived from the Tauc plot.

Photocatalytic CO_2 conversion

Photocatalytic CO_2 conversion was carried out in a Pyrex photoreactor (volume 50 mL). 1 wt% Pt was deposited over the K-CN/DFNS sample by a chemical reduction method using $NaBH_4$ as a reducing agent. (1 wt%) Pt/K-CN/DFNS sample (15 mg) was mixed with a small amount of water to form a paste and spread over the flat bottom of the reactor, having an area of 2.5 cm^2. Then the reactor was dried at 80 °C in an oven for 30 min. After this, CO_2 was passed through a water bubbler to bring a mixture of CO_2 and H_2O vapor into the photoreactor for 1 h at a flow rate of 200 mL min^{-1}. The reactor was irradiated with visible light (wavelengths 385–740 nm) using a 300 W xenon lamp (MAX 303 Asahi Spectra Co. Ltd). The output power of the lamp was adjusted to deliver 318 mW cm^{-2} at the reactor. The photograph of the experimental setup is given in Fig. S2 (ESI†). Hydrogen and methane yields were monitored by gas chromatography (Agilent 7890B, Agilent Technologies) equipped with a thermal conductivity detector (TCD) and a flame ionization detector (FID). To compare the photocatalytic activity of the photocatalyst, the total consumed electron number (TCEN) was calculated. The methane generation requires 8 electrons. The formula used for the calculation of TCEN is as follows:

$$\mathrm{TCEN} = \frac{\sum \left(C_{\mathrm{product}} \times n_{\mathrm{electrons}}\right) \times V_{\mathrm{reactor}}}{m_{\mathrm{cat}} \times t_{\mathrm{irr}}} \quad (4)$$

$C_{product}$ is the concentration of the product, $n_{electron}$ is the number of electrons involved in the conversion of CO_2 into methane, m_{cat} is the catalyst amount in g and t_{irr} is the time of irradiation in h.

To confirm that the hydrocarbon products are generated by the reduction of CO_2, isotopically labeled experiments were carried out. For this experiment, $^{13}CO_2$ was used as a reactant. The generated gaseous products after the reaction were analyzed by using GC coupled with mass spectrometry (Agilent 7890B, Agilent Technologies). For GC-MS analysis, helium was used as the carrier gas and an Agilent hybrid column CP7430 as the stationary phase.

Results and discussion

g-C_3N_4 is a potential candidate for photocatalytic CO_2 conversion. However, low surface area, the high recombination rate of charge carriers and limited light absorption in the visible region affect its photocatalytic properties. In our previous publication, to overcome these issues, we coated g-C_3N_4 over a high surface area support DFNS (CN/DFNS).[20] It showed seven times better hydrogen generation as compared to the pristine g-C_3N_4. The enhancement in photocatalytic activity was attributed to the high surface area, extended visible light absorption in the 450–650 nm range and improved charge separation due to the formation of an interface between DFNS and g-C_3N_4. The samples were further tested for CO_2 conversion. Unfortunately, it showed hydrogen as a major product and a low yield of methane. To improve its CO_2 conversion process, increase the selectivity towards CO_2 reduction products and suppress hydrogen generation, in this work, potassium ions were doped into the matrix of g-C_3N_4 loaded over DFNS (K-CN/DFNS).

For the synthesis of K-CN/DFNS, KOH-treated melamine was mixed with DFNS and placed in a vacuum-sealed quartz tube and then heated at 400 °C for 2 h and 550 °C for 2 h. The amount of potassium was varied by changing the KOH amount from 3.2 to 45.5 wt% of melamine. The morphology of the samples was analyzed by SEM (Fig. 1). The SEM images of DFNS showed the presence of a fiber-like morphology with particle size in the range of 300–500 nm, whereas that of the CN/DFNS and K-CN/DFNS samples revealed that the layers of g-C_3N_4 were grafted over the DFNS nanosheets, giving it a complete sphere-shape appearance (Fig. 1). The amount of potassium and g-C_3N_4 content in the sample was evaluated using EDX analysis (Table 1). The amount of potassium varied from 0.74, 6.06 and 18.9 wt% with respect to g-C_3N_4 for the K-CN/DFNS-1, K-CN/DFNS-2 and K-CN/DFNS-3 samples, respectively. The content of g-C_3N_4 was found to be lower in the case of K-CN/DFNS-3 as compared to the K-CN/DFNS-1 and K-CN/DFNS-2 samples.

To determine the structural modification after doping with potassium ions, the PXRD, FTIR and XPS analyses of the K-CN/DFNS samples were recorded. The PXRD pattern of g-C_3N_4 (Fig. 2a) shows peaks at 13.2° and 27.9° corresponding to the 100 and 002 planes, which were ascribed to in-planar repeating units with a period of 0.672 nm and layered staking with the interplanar spacing of 0.319 nm of aromatic systems, respectively.[25,28] K-CN/DFNS samples show a very small peak at 27.7° corresponding to the 002 plane of g-C_3N_4. The absence of other peaks at 13.2° corresponding to the 100 plane could be because of its lower content and the presence of overlapping broad peaks of amorphous SiO_2 at 22.7°.

To investigate the structural modification after doping with potassium ions, the FTIR spectra of the samples were recorded (Fig. 2b). The FTIR spectrum of g-C_3N_4 shows absorption bands

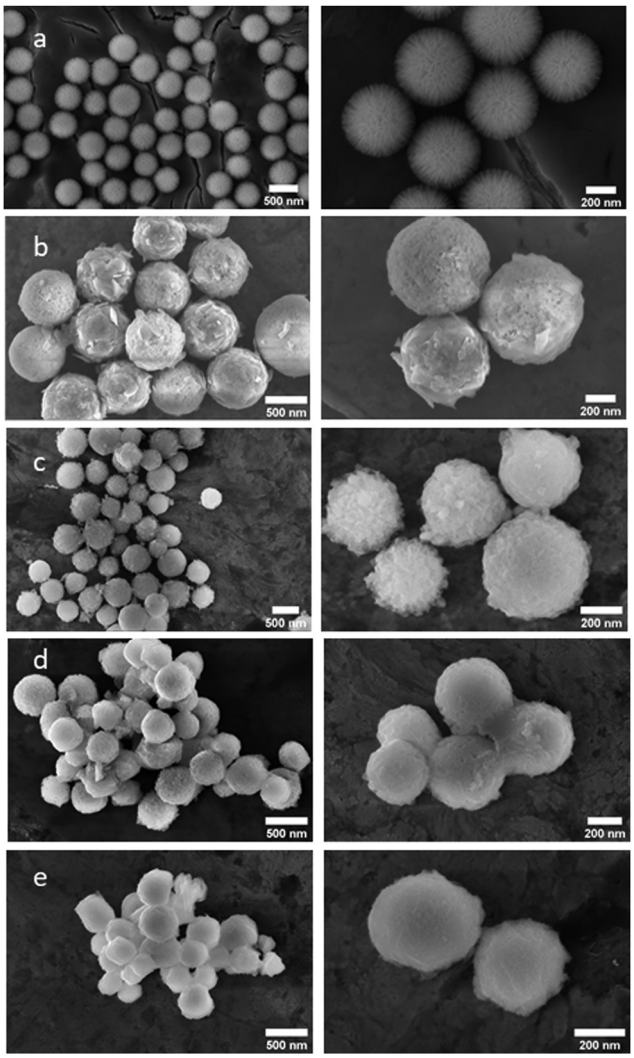

Fig. 1 The SEM images of the (a) DFNS, (b) CN/DFNS, (c) K-CN/DFNS-1, (d) K-CN/DFNS-2 and (e) K-CN/DFNS-3 samples (images from left to right indicate low resolution and high-resolution images).

at 810 and 890 cm^{-1} corresponding to the breathing mode of heptazine rings and the deforming mode of NH groups, respectively.[29] The absorption bands observed in the range of 1200–1700 cm^{-1} correspond to stretching modes of the CN heterocycle.[29] The absorption band at 1641 cm^{-1} corresponds to the C=N stretching vibration mode. Also, the absorption bands characteristic of aromatic C–N stretching were observed at 1247, 1326, 1432 and 1565 cm^{-1}. The broad band in the range of 3000–4000 cm^{-1} attributed to stretching modes of the terminal $-NH_2$ or –NH groups arises due to the presence of uncondensed amine groups and the adsorbed water molecules.[18,29] Also, a small absorption band is observed at 2145 cm^{-1}, which might correspond to the C≡N (cyano) group. The FTIR spectrum of DFNS shows absorption bands at 1097 and 1192 cm^{-1} corresponding to transverse optical (TO) and longitudinal optical (LO) modes of the asymmetric stretching of the Si–O–Si bond, respectively.[30] The weak absorption band at 966 cm^{-1} is attributed to Si–OH or Si–O-stretching and the absorption band at 807 cm^{-1} is due to Si–O–Si symmetric stretching.[30,31] The band around 1638 cm^{-1} corresponds to bending vibrations of -OH and the broadband centered around 3400 cm^{-1} belongs to -OH and the adsorbed H_2O molecules.[20,30] The K-doped samples and undoped sample show the characteristic FTIR absorption bands of both DFNS and g-C_3N_4.

It is found that the peak at 2180 cm^{-1} corresponds to the asymmetric stretching mode of the cyano group and increases with an increase in the potassium content from 1 to 6 wt%. The cyano group appears as a result of incomplete polymerization.[32] The excess KOH may prevent the polymerization of melamine, leading to defects in the K-doped samples. Also, the peak at 966 cm^{-1} corresponding to the Si–OH stretching disappeared in the case of the K-CN/DFNS-2 and K-CN/DFNS-3 samples, which might be due to the C–N–Si linkages that formed between Si–OH and $-NH_2$ groups of g-C_3N_4, which was verified by the solid-state ^{13}C and ^{1}H NMR study in our previous publication.[20] In the case of K-CN/DFNS-3, the weak absorption band in the region of 1200–1700 cm^{-1} does not appear prominently because of the lower loading of g-C_3N_4.

Furthermore, to learn more about the oxidation state of different elements and the interaction between potassium ions and g-C_3N_4, the XPS spectra of CN/DFNS, K-CN/DFNS-2 and K-CN/DFNS-2-used samples were analyzed. A survey scan of CN/DFNS shows the presence of C, N, O and Si on the surface, while K-CN/DFNS shows the existence of C, N, O, Si and K elements.

Fig. 2c shows a high-resolution spectrum of C 1s, which was deconvoluted into three peaks, namely 284.6, 286.9 and 287.9 eV, which could be assigned to the adventitious carbon, C–NH_x species, and sp^2 hybridized carbon $N{=}C{-}(N)_2$, respectively.[19] An increase in the area of the peak at 287.9 eV indicates the higher amount sp^2 hybridized carbon $N{=}C{-}(N)_2$ of g-C_3N_4 in

Table 1 Potassium content by EDX analysis, g-C_3N_4 content by TGA, bandgap measurement by UV-Visible DRS and surface area and pore volume by N_2 BET surface area analysis

Sample	Amount of potassium with respect to g-C_3N_4 by EDX (wt%)	Amount of g-C_3N_4 from TGA[a] (wt%)	Bandgap measurement by UV-Visible DRS (eV)	Surface area ($m^2\ g^{-1}$)	Pore volume ($cm^3\ g^{-1}$)
DFNS	—	—	—	622	0.719
g-C_3N_4	—	—	2.70	15	0.05
CN/DFNS	—	21.9	2.76	150	0.163
K-CN/DFNS-1	0.74	19.8	2.74	88	0.158
K-CN/DFNS-2	6.06	13.3	2.69	55	0.062
K-CN/DFNS-3	18.9	2.7	2.80	79	0.086

[a] Amount of g-C_3N_4 calculated from the weight loss in the region of 220–670 °C in the thermogram.

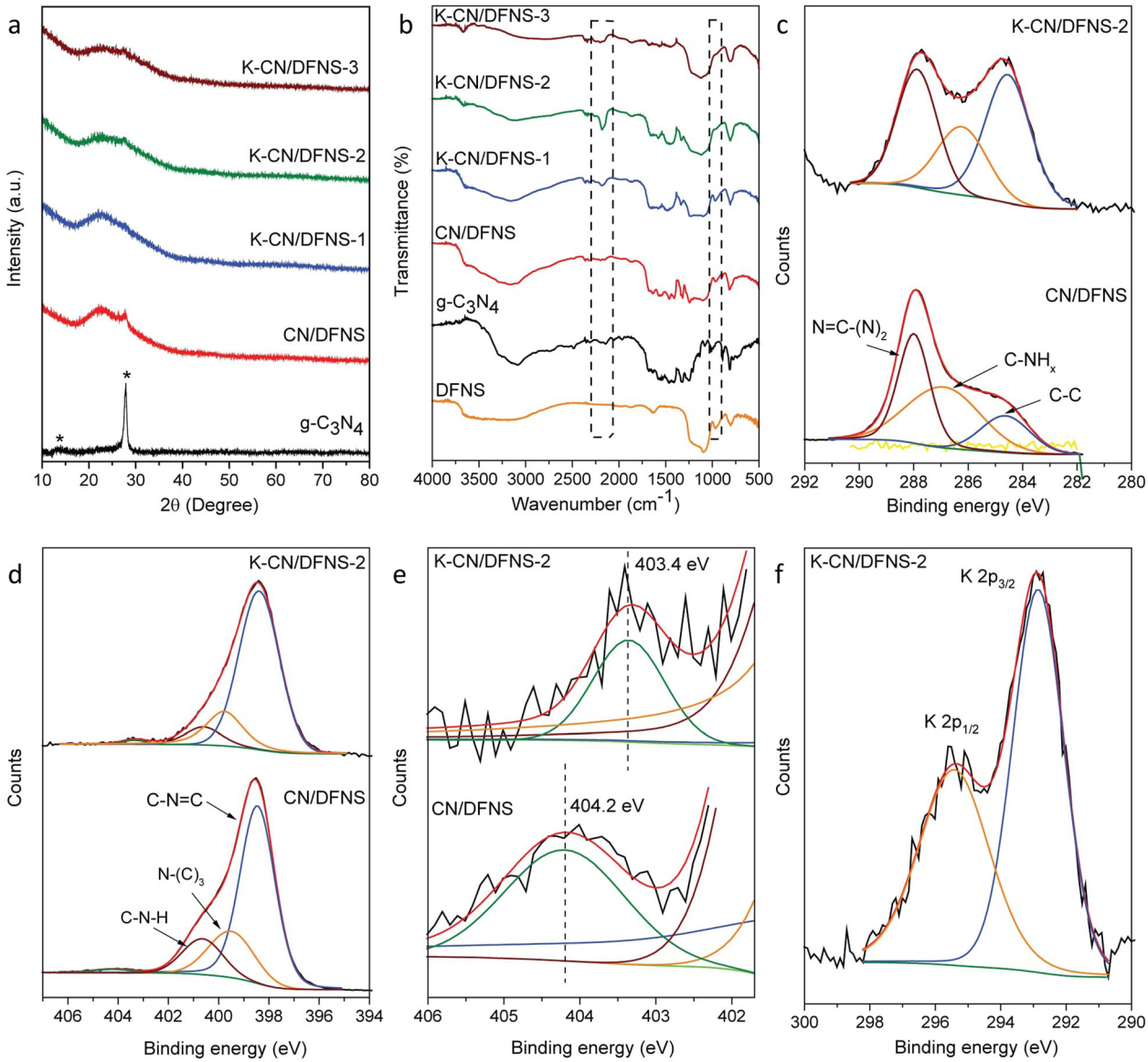

Fig. 2 (a) The PXRD patterns and (b) FTIR spectra of DFNS, g-C_3N_4, CN/DFNS, K-CN/DFNS-1, K-CN/DFNS-2 and K-CN/DFNS-3. The high-resolution XPS spectra of (c) C 1s and (d) N 1s, and (e) enlarged views of the peaks at 403 eV of N 1s and (f) K 2p of the CN/DFNS and K-CN/DFNS-2 samples (* mark the planes of g-C_3N_4).

CN/DFNS as compared to the K-CN/DFNS-2 sample. This can be correlated with the higher amount of g-C_3N_4 in CN/DFNS than in the K-CN/DFNS-2 sample.

The high-resolution N 1s spectra of the samples were deconvoluted into four peaks (Fig. 2d). The peaks appeared at 398.5, 399.5, 400.6 and 404.2 eV. The peak at 398.5 eV corresponds to the sp^2 N present in triazine rings, *i.e.* C–N=C bonds,[19] while the peaks at 399.5 and 400.6 eV correspond to the tertiary nitrogen group N–$(C)_3$ and amino group present due to incomplete polymerization, respectively.[19] The peak appearing at 404.2 eV is ascribed to the charging effect of π excitations of the C–N conjugated system.[33] The peak at 404.2 eV in CN/DFNS shifted to 403.4 eV in the potassium-doped g-C_3N_4 sample (Fig. 2e). This indicates that the damage of the π electrons might be due to the disorder in the structure of g-C_3N_4.[19] Not much considerable shift was observed with other types of nitrogen species present in the K-CN/DFNS sample.

Peaks at binding energy 292.8 and 295.4 eV in the K-CN/DFNS sample were assigned to K $2p_{3/2}$ and K $2p_{1/2}$, respectively (Fig. 2f). These peaks could be due to the existence of K–N bonds.[16] Also, the presence of the K 2s peak at 377.8 eV confirms the existence of K–N bonds (Fig. S3a, ESI†).[16,34] The high-resolution O 1s spectrum shows peaks at positions of 532.6 and 533.7 eV originating from Si–O–Si bonds of silica and water molecules adsorbed on the surface, respectively (Fig. S3b, ESI†).[23,35] The peak at binding energy of 103.4 eV corresponds to the Si 2p of the siloxane framework of DFNS (Fig. S3c, ESI†).[23]

Thermogravimetric analysis of the sample was carried out to study the thermal stability of the material. TGA analysis from

30–800 °C in the presence of air was carried out (Fig. 3a). The thermogram of DFNS shows a weight loss in the region of 43–104 °C, corresponding to the loss of adsorbed water molecules. Pristine g-C_3N_4 showed weight losses at 220–346 °C and 448–711 °C corresponding to the weight losses due to the decomposition of unreacted melamine or melam and decomposition of g-C_3N_4.[36,37] The thermogram of CN/DFNS showed weight losses in three steps. Step I: 34–132 °C corresponded to the weight loss due to physically adsorbed water. Step II: 132–283 °C was attributed to the weight loss due to the decomposition of residual intermediate products formed during the reaction. Step III: 310–670 °C was attributed to the thermal decomposition of g-C_3N_4.[20] The thermograms of the K-CN/DFNS-1, K-CN/DFNS-2 and K-CN/DFNS-3 samples also show significant weight losses in two different regions. The weight loss occurred in two steps. Step I: 40–115 °C was attributed to the adsorbed water on the surface. Step II: 220–600 °C corresponded to the decomposition of g-C_3N_4. The offset temperature was found to increase from 593 °C to 749 °C with the increase in the potassium content.

N_2 sorption analysis of K-CN/DFNS was performed to understand the textural properties and it showed a Type IV isotherm with hysteresis, indicating the mesoporous nature of the samples (Fig. S4 and S5, ESI†). The pores in the DFNS arise due to the gap between the fibres. CN/DFNS coated with 21.9 wt% of g-C_3N_4 shows a surface area of 150 $m^2\ g^{-1}$ lower than that of DFNS (622 $m^2\ g^{-1}$) but higher than g-C_3N_4 (15 $m^2\ g^{-1}$). On the increase in the potassium content, the surface area varied from 88, 55 and 79 $m^2\ g^{-1}$ for K-CN/DFNS-1, K-CN/DFNS-2 and K-CN/DFNS-3, respectively (Table 1). The pore volumes of the samples change from 0.158, to 0.062 and 0.086 $cm^3\ g^{-1}$ for K-CN/DFNS-1, K-CN/DFNS-2 and K-CN/DFNS-3, respectively. The decrease in pore volume and surface area indicates the growth of g-C_3N_4 on the DFNS fibers and also within the pores (channels) of the DFNS. The presence of potassium resulted in the distortion of the structure of g-C_3N_4, which could have resulted in a further

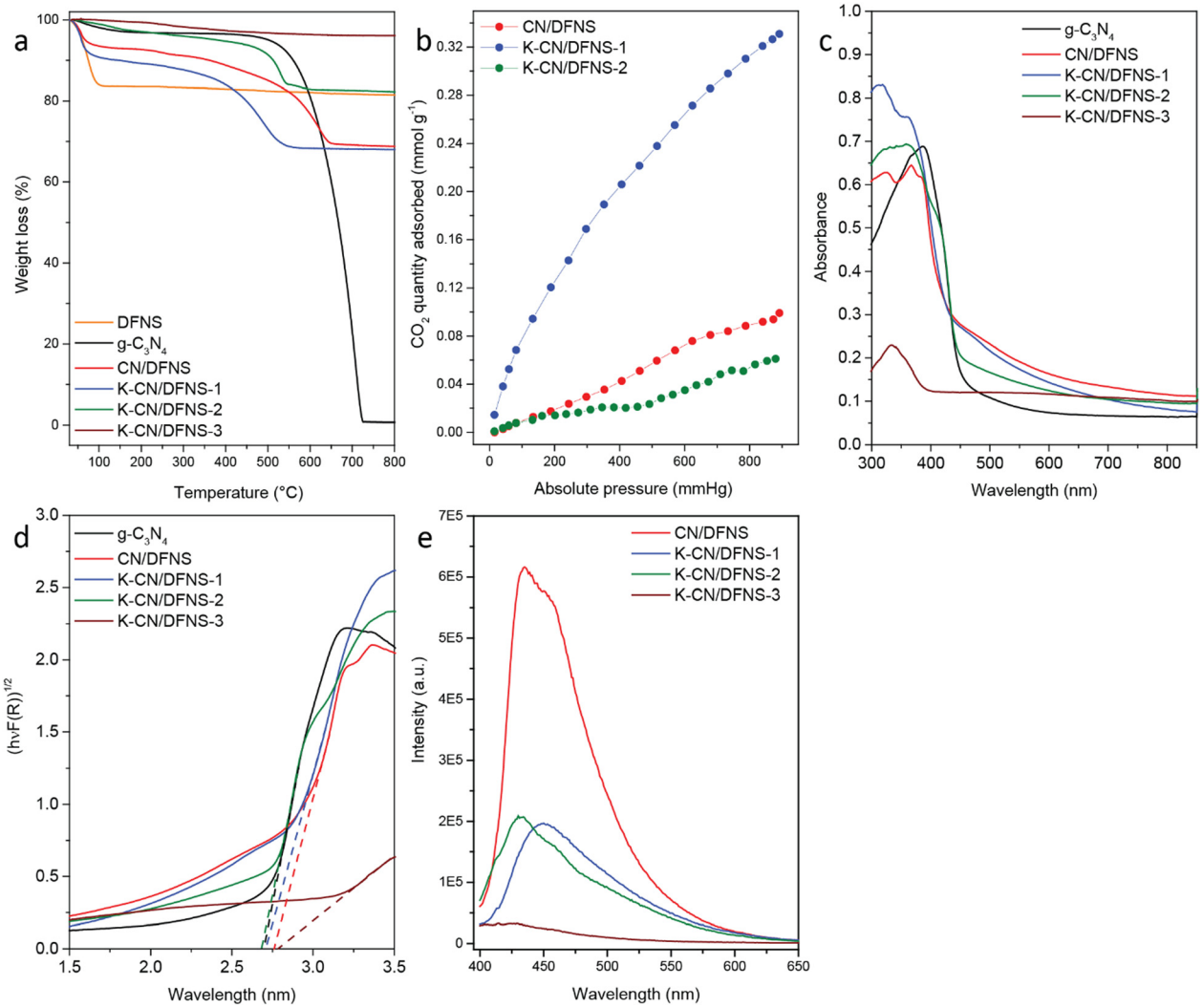

Fig. 3 (a) The TGA thermograms of the DFNS, g-C_3N_4, CN/DFNS and K-CN/DFNS samples, (b) CO_2 adsorption over CN/DFNS, K-CN/DFNS-1 and K-CN/DFNS-2, (c) the DRS spectra, (d) the Tauc plots of g-C_3N_4, CN/DFNS and K-doped samples and (e) steady-state photoluminescence spectra of CN/DFNS and K-doped samples.

decrease in the pore size and surface area as compared to the undoped sample. Due to the lower loading of g-C_3N_4 in K-CN/DFNS-3, a slight increase in surface area was observed.

CO_2 adsorption over different samples is given in Fig. 3b and Fig. S6 (ESI†). Among all the samples, K-CN/DFNS-1 has shown the highest CO_2 adsorption of 0.31 mmol g^{-1} at 780 mm Hg of CO_2 pressure and 298 K temperature. The improved adsorption could be due to increased basic sites in g-C_3N_4. These basic sites could be the increased $-NH_2$ groups in the samples. K-CN/DFNS-2 is supposed to show higher CO_2 adsorption as it has a higher content of potassium ions, around 6 wt%. However, it exhibits lower adsorption of CO_2. This could be due to the incomplete polymerization of g-C_3N_4, as evident from the presence of the cyano group, which might result in a decrease in the amino groups in the sample. The adsorption of CO_2 in the cases of CN/DFNS and K-CN/DFNS-2 could be due to the presence of pyridinic nitrogen and terminal amino groups.

The optical properties of the samples were evaluated by recording the UV-Visible DRS absorption spectra of the samples (Fig. 3c). The bandgap of the samples was calculated using Tauc plots (Fig. 3d) and tabulated in Table 1. The bandgap of pristine g-C_3N_4 was found to be 2.70 eV, while that of CN/DFNS was found to be 2.76 eV (Fig. 3c). CN/DFNS shows extended absorption in the range of 450–650 nm due to n to π^* transition resulting from the distortion in the structure of g-C_3N_4.[38] This distortion could be due to the formation of C–N–Si linkages between DFNS and g-C_3N_4 or the confined growth of g-C_3N_4 within the pores of DFNS.[20] With the increase in the potassium content, the bandgap increases. The bandgap was found to be 2.71, 2.68 and 2.78 eV for K-CN/DFNS-1, K-CN/DFNS-2 and K-CN/DFNS-3, respectively. The bandgap value is found to be slightly lower for K-CN/DFNS-2. The lower content of g-C_3N_4 in the case of K-CN/DFNS-3 resulted in the generation of thin sheets of g-C_3N_4 grafted over DFNS. This might have resulted in the blueshift of the bandgap and less absorption of light. Along with the decrease in the bandgap on increasing the loading of potassium ions until 6 wt%, the absorption in the region of 450–650 nm increases. This absorption in the region of 450–650 nm occurs due to n $\rightarrow$ π^* transition.[38] These n $\rightarrow$ π^* transitions are forbidden in perfectly symmetric and planar units.[17] This transition becomes prominent with the increasing disorder in the structure of g-C_3N_4. In the case of doped samples, the presence of potassium ions inhibits the polymerization of g-C_3N_4, as evident from the presence of the cyano group in the FTIR spectra. This indicates that the presence of potassium ions not only affects the structural and thermal properties but also affects the electronic and optical properties of g-C_3N_4.

To gain insight into the separation of charge carriers, the steady-state and time-resolved photoluminescence spectra were recorded. The samples were excited at 380 nm and the emission spectra were recorded. Fig. 3e shows the steady-state photoluminescence spectra of the CN/DFNS and K-CN/DFNS samples. It was observed that the potassium-doped samples showed low emission intensity as compared to the CN/DFNS. This infers that the rate of radiative recombination of charges is low in the K-CN/DFNS samples as compared to CN/DFNS. K-CN/DFNS-3 (18.9 wt% potassium) showed the lowest emission intensity, while its photocatalytic activity is low. CN/DFNS showed a broad emission peak centered at 434 nm, while in the case of the K-CN/DFNS samples, the emission peak was blue shifted. These results are in concurrence with the UV-Visible DRS spectra, where the bandgaps of the potassium-doped (6 wt% and 18.9 wt%) samples were found to be higher than that of CN/DFNS.

To further understand the lifetimes of charge carriers, time-resolved decay profiles were recorded. The samples were excited at 395 nm and decay profiles were recorded. The lifetime decay profile was fitted with the tri-exponential fitting decay eqn 1 (Table 2). In the case of doped samples, the average lifetimes were found to increase with an increase in the potassium amount. The contribution from the shortest lifetime (τ_1) increases with an increase in the potassium content. This indicates the effective transfer of charges to the impurity states or defect centers created after doping with potassium ions. This lowering in average lifetime as compared to g-C_3N_4 might be due to the increased charge recombination by the non-radiative pathway. This was also evident from the lowering of the PL intensity in the steady-state experiments.

Photocatalytic CO_2 conversion using K-CN/DFNS

Photocatalytic CO_2 conversion of the samples was evaluated under visible light illumination (Fig. 4). Moist CO_2 was passed over 15 mg of K-CN/DFNS/Pt (1 wt% Pt was pre-deposited by chemical reduction method) in a batch reactor for 1 h and then irradiated under a 300 W Xe lamp (384–750 nm, 318 mW cm^{-2}). Quantification of H_2 and CH_4 generated after 4 h of reaction was monitored by GC-TCD-FID. CN/DFNS showed only hydrogen generation, whereas in the case of potassium-doped samples, no H_2 generation was observed. The optimum amount of potassium content is needed to get the maximum photocatalytic activity. In this case, 6 wt% potassium-doped g-C_3N_4 coated over DFNS shows the highest activity and preferential CO_2 conversion over hydrogen generation. The highest methane yield observed was 1.7 μmol g^{-1} of g-C_3N_4 in 4 h using K-CN/DFNS-2 (6 wt% of potassium ion). The methane generation observed over the K-CN/DFNS-2 sample was found to be nearly three times higher than that of the pristine g-C_3N_4. The overall activity for methane generation was estimated from total consumed electrons using eqn (4) (TCEN). The TCEN for different samples were found to be 1.14, 0.64, and 3.4 μmol g^{-1} h^{-1} for the g-C_3N_4, K-CN/DFNS-1 and K-CN/DFNS-2, respectively. This enhancement in activity could be attributed to the improved light absorption, enhanced separation of charge carriers and suitable structural changes brought by the presence of the optimum amount of potassium.

Table 2 Lifetime measurements by time resolved photoluminescence

Sample name	τ_1 (ns)	A_1	τ_2 (ns)	A_2	τ_3 (ns)	A_3	χ^2	τ_{avg} (ns)
g-C_3N_4	0.841	0.406	2.509	0.484	7.445	0.11	1.08	3.97
CN/DFNS	0.525	0.581	1.909	0.354	6.927	0.064	1.02	3.17
K-CN/DFNS-1	0.122	0.791	1.271	0.166	5.27	0.043	1.694	1.45
K-CN/DFNS-2	0.048	0.895	0.821	0.08	4.236	0.025	2.926	2.35
K-CN/DFNS-3	0.018	0.92	0.988	0.061	4.929	0.02	1.004	3.11

Note: For all the samples excitation wavelength was 380 nm and emission wavelength was around 434 nm.

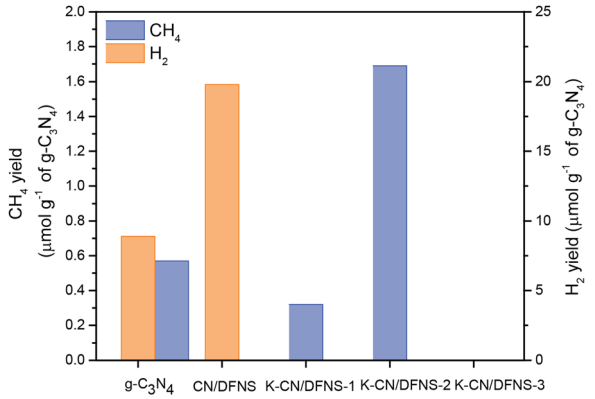

Fig. 4 Yields of CO_2 conversion products (methane) and hydrogen in 4 h using g-C_3N_4, CN/DFNS, and K-CN/DFNS samples in the presence of 1 wt% Pt as a cocatalyst under visible light illumination (385–740 nm).

On the contrary, despite having lower CO_2 adsorption, K-CN/DFNS-2 has shown better photocatalytic activity. CO_2 adsorption is not the only criterion that defines the better yield in photocatalytic CO_2 conversion. Other factors such as light absorption and the separation of charge carriers also play important roles. Therefore, in the case of K-CN/DFNS-2 the redshift in the absorption edge and the improved separation of charge carriers are the factors that influence the photocatalytic activity. In spite of having a greater average lifetime and extended absorption in the visible region, K-CN/DFNS-3 has not shown any conversion. This could be attributed to the lower amount of g-C_3N_4 loading over DFNS and increased bandgap, which further obstruct the light absorption properties and thus result in the lower amount of charge carrier generation.

To confirm the source of the carbon, isotope-labeled experiments were performed using $^{13}CO_2$ and the products were analyzed by GC-MS. The mass fragmentation is given in Fig. S7 (ESI†). A signal at m/z = 17 corresponds to $^{13}CH_4$. This confirms that methane is generated from the reduction of CO_2. In addition to this, the sample recovered after the CO_2 conversion reaction, K-CN/DFNS-2-used, was also studied by XPS (Fig. S8, ESI†). Not much change in the spectrum was observed. This implies that the catalyst remains stable after the photocatalytic reaction.

It is difficult to compare the yields of the products because of various experimental conditions such as intensity of the light source, amount of catalyst and water, reactor design, and distance between the reactor and light source. Very few reports are found on potassium-doped g-C_3N_4 systems.[18,19] The methane yield reported in the current manuscript is lower than that in the reported literature on potassium-doped g-C_3N_4 (Table S1, ESI†). However, the activity for CO_2 conversion using K-CN/DFNS was found to be higher than those of some of the doped g-C_3N_4 systems reported in the literature.[39–42]

This is the first time that the role of DFNS as a support and the effects of various amount contents of potassium ion on the photocatalytic property of g-C_3N_4 are studied. In this case, CN/DFNS, which showed a generation of primary hydrogen, was structurally modified by doping with potassium to tune the selectivity for CO_2 reduction. The structural changes brought by doping of potassium ions, such as generation of a cyano group, formation of K–N bonds and the interface between DFNS and g-C_3N_4 through C–N–Si bonds, modification in the absorption spectrum and enhancement in charge carrier dynamics, have positively contributed to the improvement in activity and selectivity of the potassium-doped samples.

Band alignment and mechanism of photocatalytic CO_2 conversion

To understand the band structure and relative position of CB and VB, the valence band XPS spectra were recorded. The valence band XPS spectra of K-CN/DFNS-2 sample shows a

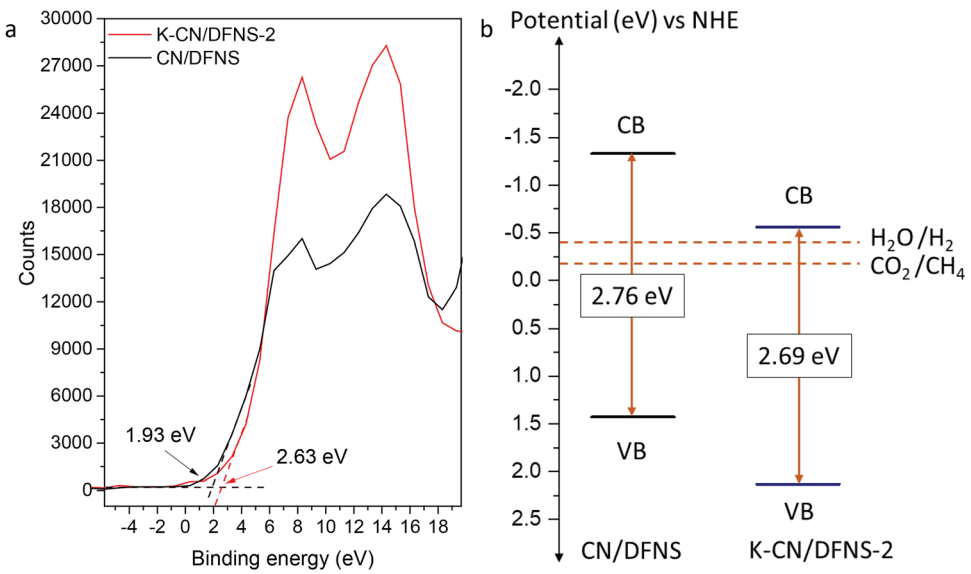

Fig. 5 (a) The valence band XPS spectra of CN/DFNS and K-CN/DFNS-2 and (b) energy diagram showing the positions of the conduction band (CB) and valence band (VB) of CN/DFNS and K-CN/DFNS-2 samples derived from the valence band XPS spectra and bandgap.

slight shift in the valence band edge as shown in Fig. 5a. The structural changes brought by the presence of potassium ions, such as the existence of a cyano group and the disordered structure of g-C_3N_4 might have resulted in a shift in the position of the conduction and valence band edge.

From the valence band XPS spectra, the differences between the Fermi level and valence band maximum (ΔE) of CN/DFNS and K-CN/DFNS-2 were found to be 1.93 and 2.63 eV, respectively. E_{VB} was calculated using eqn (2). The valence band (E_{VB}) of CN/DFNS and K-CN/DFNS-2 were found to be 1.43 and 2.13 eV, respectively. The conduction band (E_{CB}) was calculated using the bandgap value estimated from E_{VB} and the Tauc plot (Table 1 and Fig. 3d). The E_{CB} values of CN/DFNS and K-CN/DFNS-2 were found to be −1.33 and −0.56 eV, respectively. Fig. 5b shows the positions of the conduction and valence bands in the CN/DFNS and K-CN/DFNS-2 samples.

The thermodynamic potential for the generation of methane and hydrogen are as follows:[43]

$$CO_2 + 8H^+ + 8e^- \rightarrow CH_4 + 2H_2O \quad E^0 = -0.24 \text{ V } vs. \text{ NHE}$$

$$2H^+ + 2e^- \rightarrow H_2 \quad E^0 = -0.41 \text{ V } vs. \text{ NHE}$$

Due to the presence of potassium ions, both E_{CB} and E_{VB} of the K-CN/DFNS-2 samples have altered. The K-CN/DFNS-2 sample has a suitable band position for the generation of methane from CO_2 and reduction of water. The position of the CB is more negative than the standard reduction potential of CO_2, thus making its photocatalytic reduction feasible.

Lowering the conduction band potential to vary the potential of photogenerated electrons is one of the strategies to tune the product selectivity.[44] In this case, the lowering of E_{CB} of the K-CN/DFNS-2 sample by −0.77 eV as compared to that of CN/DFNS might be the reason for the improved selectivity for CO_2 conversion.

The following mechanism was predicted from the observed data: when light falls on K-CN/DFNS, an electron gets excited to the conduction band by leaving behind a hole. The photogenerated hole can oxidize water and release protons, while the electron can migrate to Pt, where it can reduce CO_2 in the presence of a proton to give methane. As compared to pristine g-C_3N_4, K-CN/DFNS-2 has shown better activity for methane generation and prohibited hydrogen generation due to the enhanced absorption of light, better separation of charge carriers, the shift of the conduction band and valence band towards positive potentials and moderate adsorption of CO_2.

Conclusions

In this work, we were able to tune the selectivity of K-CN/DFNS and preferentially reduce CO_2 over water reduction to generate hydrogen by simple potassium ion doping into the matrix of g-C_3N_4. It was observed that the potassium ion doping affected the structural, thermal, optical and electronic properties of g-C_3N_4. The SEM images confirm the grafting of the layers of potassium-doped g-C_3N_4 over DFNS. The presence of potassium ions hampers the polymerization of g-C_3N_4, which was evident from the presence of the cyano group in the FTIR spectra of the potassium-doped samples. The XPS analysis further confirms the interaction of potassium ions with the nitrogen of g-C_3N_4 and the disordered structure of g-C_3N_4. The lowering of the bandgap and the extended absorption in visible light was observed until 6 wt% of potassium ion loading. Also, the lifetime of the charge carriers increases with an increase in the potassium content. Improved productivity for CO_2 conversion and suppression of hydrogen generation reaction was found over the potassium-doped samples. Among all the samples, K-CN/DFNS-2 (with 6 wt% of potassium ion doped in g-C_3N_4) has shown the highest CO_2 conversion, with a 1.7 μmol g^{-1} of g-C_3N_4 yield of methane, in 4 h under visible light irradiation. The UV-DRS, PL, and lifetime measurement studies indicated that the improved activity and preferential CO_2 reduction over hydrogen generation were due to the extended absorption in the visible region, better separation of charge carriers, shifting of the conduction band and valence band towards positive potentials and moderate adsorption of CO_2. This study will be useful for the designing of catalysts with improved selectivity for CO_2 conversion over hydrogen generation.

Conflicts of interest

There are no conflicts to declare.

References

1 M. Khalil, J. Gunlazuardi, T. A. Ivandini and A. Umar, Photocatalytic conversion of CO_2 using earth-abundant catalysts: A review on mechanism and catalytic performance, *Renewable Sustainable Energy Rev.*, 2019, **113**, 109246.
2 L. Xu, Y. Xiu, F. Liu, Y. Liang and S. Wang, Research progress in conversion of CO_2 to valuable fuels, *Molecules*, 2020, **25**, 3653.
3 T. Kong, Y. Jiang and Y. Xiong, Photocatalytic CO_2 conversion: What can we learn from conventional COx hydrogenation?, *Chem. Soc. Rev.*, 2020, **49**, 6579–6591.
4 U. Ulmer, T. Dingle, P. N. Duchesne, R. H. Morris, A. Tavasoli, T. Wood and G. A. Ozin, Fundamentals and applications of photocatalytic CO_2 methanation, *Nat. Commun.*, 2019, **10**, 3169.
5 Z. Bi, R. Guo, X. Hu, J. Wang, X. Chen and W. Pan, Research progress on photocatalytic reduction of CO_2 based on LDH materials, *Nanoscale*, 2022, **14**, 3367–3386.
6 Y. Miao, R. Guo, J. Gu, Y. Liu, G. Wu, C. Duan and W. Pan, Oxygen vacancy-rich BiO_{2-x}: Super-active co-catalyst on g-C_3N_4 for efficient visible-light photocatalytic CO_2 reduction, *J. CO2 Util.*, 2021, **44**, 101377.
7 G. Dong, Y. Zhang, Q. Pan and J. Qiu, A fantastic graphitic carbon nitride (g-C_3N_4) material: Electronic structure, photocatalytic and photoelectronic properties, *J. Photochem. Photobiol., C*, 2014, **20**, 33–50.
8 G. Mamba and A. K. Mishra, Graphitic carbon nitride (g-C_3N_4) nanocomposites: A new and exciting generation of visible light

driven photocatalysts for environmental pollution remediation, *Appl. Catal., B*, 2016, **198**, 347–377.
9 X. Wang, K. Maeda, A. Thomas, K. Takanabe, G. Xin, J. M. Carlsson, K. Domen and M. Antonietti, A metal-free polymeric photocatalyst for hydrogen production from water under visible light, *Nat. Mater.*, 2009, **8**, 76–80.
10 D. J. Martin, K. Qiu, S. A. Shevlin, A. D. Handoko, X. Chen, Z. Guo and J. Tang, Highly efficient photocatalytic H_2 evolution from water using visible light and structure-controlled graphitic carbon nitride, *Angew. Chem., Int. Ed.*, 2014, **53**, 9240–9245.
11 S. Samanta and R. Srivastava, Catalytic conversion of CO_2 to chemicals and fuels: the collective thermocatalytic/photocatalytic/electrocatalytic approach with graphitic carbon nitride, *Mater. Adv.*, 2020, **1**, 1506–1545.
12 L. Jiang, X. Yuan, Y. Pan, J. Liang, G. Zeng, Z. Wu and H. Wang, Doping of graphitic carbon nitride for photocatalysis: A review, *Appl. Catal., B*, 2017, **217**, 388–406.
13 Y. Wang, S. Zhao, Y. Zhang, J. Fang, Y. Zhou, S. Yuan, C. Zhang and W. Chen, One-pot synthesis of K-doped g-C_3N_4 nanosheets with enhanced photocatalytic hydrogen production under visible-light irradiation, *Appl. Surf. Sci.*, 2018, **440**, 258–265.
14 J. Ma, W. Zhou, X. Tan and T. Yu, Potassium ions intercalated into g-C_3N_4-modified TiO_2 nanobelts for the enhancement of photocatalytic hydrogen evolution activity under visible-light irradiation, *Nanotechnology*, 2018, **29**, 21.
15 J. Jiang, S. Cao, C. Hu and C. Chen, A comparison study of alkali metal-doped g-C_3N_4 for visible-light photocatalytic hydrogen evolution, *Chin. J. Catal.*, 2017, **38**, 1981–1989.
16 S. Hu, F. Li, Z. Fan, F. Wang, Y. Zhao and Z. Lv, Band gap-tunable potassium doped graphitic carbon nitride with enhanced mineralization ability, *Dalton Trans.*, 2015, **44**, 1084–1092.
17 H. Katsumata, K. Sakakibara, I. Tateishi, M. Furukawa and S. Kaneco, Structurally modified graphitic carbon nitride with highly photocatalytic activity in the presence of visible light, *Catal. Today*, 2020, **352**, 47–53.
18 S. Wang, J. Zhan, K. Chen, A. Ali, L. Zeng, H. Zhao, W. Hu, L. Zhu and X. Xu, Potassium-doped g-C_3N_4 achieving efficient visible-light-driven CO_2 reduction, *ACS Sustainable Chem. Eng.*, 2020, **8**(22), 8214–8222.
19 Z. Sun, S. Wang, Q. Li, M. Lyu, T. Butburee, B. Luo, H. Wang, J. M. T. A. Fischer, C. Zhang, Z. Wu and L. Wang, Enriching CO_2 activation sites on graphitic carbon nitride with simultaneous introduction of electron-transfer promoters for superior photocatalytic CO_2-to-fuel conversion, *Adv. Sustainable Syst.*, 2017, **1**, 1700003.
20 S. A. Rawool, A. Samanta, T. G. Ajithkumar, Y. Kar and V. Polshettiwar, Photocatalytic hydrogen generation and CO_2 conversion using g-C_3N_4 decorated dendritic fibrous nanosilica: role of interfaces between silica and g-C_3N_4, *ACS Appl. Energy Mater.*, 2020, **3**, 8150–8158.
21 A. Maity, R. Belgamwar and V. Polshettiwar, Facile synthesis protocol to tune size, textural properties & fiber density of dendritic fibrous nanosilica (DFNS): applications in catalysis and CO_2 capture, *Nat. Protoc.*, 2019, **14**, 2177–2204.
22 V. Polshettiwar, Dendritic Fibrous Nano-Silica (DFNS): Discovery, Synthesis, Formation Mechanism, Catalysis, and CO_2 Capture-Conversion, *Acc. Chem. Res.*, 2022, **55**, 1395–1410.
23 A. K. Mishra, R. Belgamwar, R. Jana, A. Datta and V. Polshettiwar, Defects in nanosilica catalytically convert CO_2 to methane without any metal and ligand, *Proc. Natl. Acad. Sci. U. S. A.*, 2020, **117**, 6383–6390.
24 A. Maity, S. Chaudhari, J. J. Titman and V. Polshettiwar, Nanosponges of acidic amorphous aluminosilicate for catalysis, plastic degradation and CO_2 to fuel conversion, *Nat. Commun.*, 2020, **11**, 3828.
25 K. Li, F.-Y. Su and W.-D. Zhang, Modification of g-C_3N_4 nanosheets by carbon quantum dots for highly efficient photocatalytic generation of hydrogen, *Appl. Surf. Sci.*, 2016, **375**, 110–117.
26 *Principles of Fluorescence Spectroscopy*, ed., Lakowicz J. R., Springer, USA, 2006.
27 J. Huang, G. Nie and Y. Ding, Metal-free enhanced photocatalytic activation of dioxygen by g-C_3N_4 doped with abundant oxygen-containing functional groups for selective N-deethylation of Rhodamine B, *Catalysts*, 2020, **10**, 6.
28 Y. Yuan, L. Zhang, J. Xing, M. I. B. Utama, X. Lu, K. Du, Y. Li, X. Hu, S. Wang, A. Genç, R. Dunin-borkowski, J. Arbiol and Q. Xiong, High-yield synthesis and optical properties of g-C_3N_4, *Nanoscale*, 2015, **7**, 12343–12350.
29 L. Ge, F. Zuo, J. Liu, Q. Ma, C. Wang, D. Sun, L. Bartels and P. Feng, Synthesis and efficient visible light photocatalytic hydrogen evolution of polymeric g-C_3N_4 Coupled with CdS quantum dots, *J. Phys. Chem. C*, 2012, **116**, 13708–13714.
30 R. Singh, N. Bayal, A. Maity, D. J. Pradeep, J. Trébosc, P. K. Madhu, P. Lafon and V. Polshettiwar, Probing the interfaces in nanosilica-supported TiO_2 photocatalysts by solid-state NMR and in situ FTIR, *ChemNanoMat*, 2018, **4**, 1231–1239.
31 B. Lin, C. Xue, X. Yan, G. Yang, G. Yang and B. Yan, Facile fabrication of novel SiO_2/g-C_3N_4 core–shell nanosphere photocatalysts with enhanced visible light activity, *Appl. Surf. Sci.*, 2015, **357**, 346–355.
32 M. Zhang, X. Bai, D. Liu, J. Wang and Y. Zhu, Enhanced catalytic activity of potassium-doped graphitic carbonnitride induced by lower valence position, *Appl. Catal., B*, 2015, **164**, 77–81.
33 J. Yu, K. Wang, W. Xiao and B. Cheng, Photocatalytic reduction of CO_2 into hydrocarbon solar fuels over g-C_3N_4–Pt nanocomposite photocatalysts, *Phys. Chem. Chem. Phys.*, 2014, **16**, 11492–11501.
34 J. Sharma, T. Gora, J. D. Rimstidt and R. Staley, X-Ray photoelectron spectra of the alkali azides, *Chem. Phys. Lett.*, 1972, **15**, 232.
35 A. Thøgersen, J. H. Selj and E. S. Marstein, Oxidation effects on graded porous silicon anti-reflection coatings, *J. Electrochem. Soc.*, 2012, **159**(5), D276–D281.
36 Y. Zhao, Z. Liu, W. Chu, L. Song, Z. Zhang, D. Yu, Y. Tian, S. Xie and L. Sun, Large-Scale synthesis of nitrogen-rich carbon nitride microfibers by using graphitic carbon nitride as precursor, *Adv. Mater.*, 2008, **20**, 1777–1781.

37 S. C. Yan, Z. S. Li and Z. G. Zou, Photodegradation performance of g-C_3N_4 fabricated by directly heating melamine, *Langmuir*, 2009, **25**, 10397–10401.

38 M. K. Bhunia, S. Melissen, M. R. Parida, P. Sarawade, J. Basset, D. H. Anjum, O. F. Mohammed, P. Sautet, T. L. Bahers and K. Takanabe, Dendritic tip-on polytriazine-based carbon nitride photocatalyst with high hydrogen evolution activity, *Chem. Mater.*, 2015, **27**, 8237–8247.

39 Q. Huang, J. Yuab, S. Cao, C. Cui and B. Cheng, Efficient photocatalytic reduction of CO_2 by amine-functionalized g-C_3N_4, *Appl. Surf. Sci.*, 2015, **358**, 350–355.

40 K. Wang, Q. Li, B. Liu, B. Cheng, W. Ho and J. Yu, Sulfur-doped g-C_3N_4 with enhanced photocatalytic CO_2- reduction performance, *Appl. Catal., B*, 2015, **176–177**, 44–52.

41 X. Liu, P. Wang, H. Zhai, Q. Zhang, B. Huang, Z. Wang, Y. Liu, Y. Dai, X. Qin and X. Zhang, Synthesis of synergetic phosphorus and cyano groups (–C≡N) modified g-C_3N_4 for enhanced photocatalytic H_2 production and CO_2 reduction under visible light irradiation, *Appl. Catal., B*, 2018, **232**, 521–530.

42 M. Arumugam, M. Tahir and P. Praserthdam, Effect of nonmetals (B, O, P, and S) doped with porous g-C_3N_4 for improved electron transfer towards photocatalytic CO_2 reduction with water into CH4, *Chemosphere*, 2022, **286**(2), 131765.

43 J. Pan, X. Wu, L. Wang, G. Liu, G. Q. Lu and H.-M. Cheng, Synthesis of anatase TiO_2 rods with dominant reactive {010} facets for the photoreduction of CO_2 to CH_4 and use in dye-sensitized solar cells, *Chem. Commun.*, 2011, **47**, 8361–8363.

44 J. Fu, K. Jiang, X. Qiu, J. Yu and M. Liu, Product selectivity of photocatalytic CO_2 reduction reactions, *Mater. Today*, 2020, **32**, 222–243.